

Low-Temperature Exsolution of Ni–Ru Bimetallic Nanoparticles from A-Site Deficient Double Perovskites

*Original*

Low-Temperature Exsolution of Ni–Ru Bimetallic Nanoparticles from A-Site Deficient Double Perovskites / Guo, J.; Cai, R.; Cali', E.; Wilson, G. E.; Kerherve, G.; Haigh, S. J.; Skinner, S. J.. - In: SMALL. - ISSN 1613-6829. - 18:43(2022). [10.1002/smll.202107020]

*Availability:*

This version is available at: 11583/2989717 since: 2024-06-19T19:49:30Z

*Publisher:*

Wiley

*Published*

DOI:10.1002/smll.202107020

*Terms of use:*

This article is made available under terms and conditions as specified in the corresponding bibliographic description in the repository

*Publisher copyright*

(Article begins on next page)

# Low-Temperature Exsolution of Ni–Ru Bimetallic Nanoparticles from A-Site Deficient Double Perovskites

Jia Guo, Rongsheng Cai, Eleonora Cali, George E. Wilson, Gwilherm Kerherve, Sarah J. Haigh, and Stephen J. Skinner\*


Exsolution of stable metallic nanoparticles for use as efficient electrocatalysts has been of increasing interest for a range of energy technologies. Typically, exsolved nanoparticles show higher thermal and coarsening stability compared to conventionally deposited catalysts. Here, A-site deficient double perovskite oxides,  $\text{La}_{2-x}\text{NiRuO}_{6-\delta}$  ( $x = 0.1$  and  $0.15$ ), are designed and subjected to low-temperature reduction leading to exsolution. The reduced double perovskite materials are shown to exsolve nanoparticles of 2–6 nm diameter during the reduction in the low-temperature range of 350–450 °C. The nanoparticle sizes are found to increase after reduction at the higher temperature (450 °C), suggesting diffusion-limited particle growth. Interestingly, both nickel and ruthenium are co-exsolved during the reduction process. The formation of bimetallic nanoparticles at such low temperatures is rare. From the in situ impedance spectroscopy measurements of the double perovskite electrode layers, the onset of the exsolution process is found to be within the first few minutes of the reduction reaction. In addition, the area-specific resistance of the electrode layers is found to decrease by 90% from 291 to 29  $\Omega \text{ cm}^2$ , suggesting encouraging prospects for these low-temperature rapidly exsolved Ni/Ru alloy nanoparticles in a range of catalytic applications.

## 1. Introduction

Metal nanoparticle catalysts are widely applied in many fields as the active sites for electrochemical reactions in renewable energy devices,<sup>[1,2]</sup> catalysis,<sup>[3,4]</sup> and sensing.<sup>[5]</sup> Compared to monometallic catalysts, bimetallic catalysts have been found to have higher catalytic performance through tuning of the electronic and structural features of the nanoparticles.<sup>[6–8]</sup> However, poor stability has limited the application of conventionally impregnated or infiltrated metal nanoparticles due to their coarsening

J. Guo, E. Cali, G. E. Wilson, G. Kerherve, S. J. Skinner  
Department of Materials  
Imperial College London  
Exhibition Road, London SW7 2AZ, UK  
E-mail: s.skinner@imperial.ac.uk

R. Cai, S. J. Haigh  
Department of Materials  
University of Manchester  
Manchester M13 9PL, UK

 The ORCID identification number(s) for the author(s) of this article can be found under <https://doi.org/10.1002/smll.202107020>.

© 2022 The Authors. Small published by Wiley-VCH GmbH. This is an open access article under the terms of the Creative Commons Attribution License, which permits use, distribution and reproduction in any medium, provided the original work is properly cited.

DOI: 10.1002/smll.202107020

and agglomeration, which is caused by the weak interaction between the metal catalysts and their supports, in addition to carbon and sulfur poisoning that deactivates the catalysts.<sup>[9,10]</sup> This has generated great research interest in the development of more stable and effective catalysts.

In recent decades, redox exsolution, in which metal species segregate from the oxide bulk to the surface and form nanoparticles in reducing atmospheres, has become an attractive alternative to the conventional methods of catalyst fabrication.<sup>[11,12]</sup> After a single thermal reduction treatment, the diffusion of reducible metal ions from the bulk to the surface, or exsolution, forms epitaxially grown nanoparticles that partially socket into the parent oxides.<sup>[13–15]</sup> The robust interaction of the exsolved particles and the parent oxide support increases coking and coarsening resistance.<sup>[13,16]</sup> Besides, some studies found that the exsolved nanoparticles were able to redissolve into the oxide lattice

in a higher oxygen partial pressure atmosphere and regenerate again through reduction, extending the lifetime of the catalysts. For example, exsolved Ni nanoparticles would fully reincorporate into the  $\text{LaFe}_{1-x}\text{Ni}_x\text{O}_{3\pm\delta}$  lattice after calcination at  $T \geq 800$  °C and self-regenerate nanoscale particles even after eight redox cycles.<sup>[17]</sup> Another intriguing aspect of exsolution is that the strain imposed by the “socketed” structure provides tunability of catalytic activity and electronic conductivity.<sup>[18,19]</sup> Hence, the highly efficient, single-step preparation of the nanoscale metal catalysts has been intensively studied in recent years, including the exsolution of bimetallic catalysts.<sup>[10]</sup>

The exsolution of bimetallic nanoparticles from bulk oxides has gained increasing attention in the last decade.<sup>[10]</sup> Kapokova et al. reported that Ni–Fe alloy nanoparticles were formed by reducing  $\text{LnFe}_{0.7}\text{Ni}_{0.3}\text{O}_{3-\delta}$  ( $\text{Ln} = \text{La}, \text{Pr}, \text{Sm}$ ) perovskite in  $\text{H}_2$  at 600 °C, which showed high catalytic activity and stability for dry methane reforming.<sup>[20]</sup> During the dry reforming reaction, the transportation of oxygen species between the Ni–Fe phase and Ln–Fe–O perovskite played a vital role. Similar materials have been applied as electrocatalysts in solid oxide cells (SOCs), showing enhanced electrochemical performance and durability in high-temperature operation.<sup>[21–23]</sup> Exsolved nanoparticles with different compositions, such as Fe–Co and Ni–Co alloy nanoparticles, were also intensively investigated in the area of SOC<sub>s</sub>,<sup>[24,25]</sup> methane dry reforming,<sup>[26]</sup> and

supercapacitors.<sup>[27]</sup> However, the exsolution of bimetallic nanoparticles often requires high-temperature treatment, which hinders the application of exsolution processes. For nanoparticles generated through in situ exsolution for SOC applications, the high-temperature requirements would limit the operating temperature to greater than the exsolution temperature, typically in excess of 800 °C. As there is a drive to lower SOC operating temperatures, this is a significant potential limitation. Similarly, for low-temperature applications, the preheat treatment at high temperature to generate electrode layers from nanomaterials could decrease the specific surface area of the parent oxides and the active metal nanoparticles by grain growth and coarsening, deactivating the catalysts/electrocatalysts.<sup>[28]</sup>

Low-temperature exsolution is therefore attractive, especially for noble metal catalysts, due to the tendency of the noble-metal-doped matrix to decompose in reducing conditions.<sup>[18]</sup> For example, Jang et al.<sup>[28]</sup> reported exsolution of Ir nanoparticles from WO<sub>3</sub> in the temperature range of 300–500 °C, achieved by the external dopant-driven phase transition. Naem et al.<sup>[29]</sup> demonstrated the exsolution of Ru metal from Ln<sub>2</sub>Ru<sub>0.2</sub>Ce<sub>1.8</sub>O<sub>7</sub> (Ln = Sm, Nd, La) by studying X-ray photoelectron spectroscopy (XPS) spectral evolution in the temperature range of 300–500 °C. Buharon et al.<sup>[30]</sup> observed Ni–Pd core–shell nanoparticles exsolved from a LaFe<sub>0.6</sub>Ni<sub>0.3</sub>Pd<sub>0.1</sub>O<sub>3-δ</sub> perovskite after reduction in 5%H<sub>2</sub>/N<sub>2</sub> at 550 °C using scanning transmission electron microscopy (STEM) and energy dispersive X-ray (EDX) spectroscopy. They also demonstrated the formation of Ni–Pd core–shell nanoparticles at 350 °C by measuring H<sub>2</sub> consumption in temperature-programmed reduction experiments.

Usually, guest elements are substituted into the host oxides as the reactant for exsolution. Perovskite oxides (ABO<sub>3</sub>) and their variants (AA'B<sub>2</sub>O<sub>6</sub>, A<sub>2</sub>BB'O<sub>6</sub> double perovskites and A<sub>n+1</sub>B<sub>n</sub>O<sub>3n+1</sub> Ruddlesden–Popper phases) with substitution on the B-sites are mainly studied as the parent oxides, benefiting from their flexible and tunable structures. Ruthenium and nickel, as two of the most promising metal catalysts, have been reported to exhibit excellent catalytic activity and enhanced chemical stability toward hydrogen production,<sup>[31,32]</sup> hydrogen storage,<sup>[6,33,34]</sup> methanation,<sup>[7,31]</sup> and oxygen reduction.<sup>[35]</sup> In this work, we have developed and investigated a new system, B-site-double perovskite, La<sub>2-x</sub>NiRuO<sub>6-δ</sub> (x = 0.1 and 0.15, denoted as L2-xNR) for reduction and exsolution at a lower temperature range. A-site deficiency was also introduced into the lattice to facilitate exsolution. Scanning electron microscopy (SEM), transmission electron microscopy (TEM), STEM, EDX, X-ray diffraction (XRD), thermogravimetric analysis (TGA), and XPS were utilized to characterize the double perovskites before and after the exsolution process. We show that A-site deficient samples successfully exsolved nanoparticles in the low-temperature reduction range of 350–450 °C. The nanoparticles exsolved at 450 °C were identified to be a Ni–Ru alloy. In situ electrochemical impedance spectroscopy (EIS) indicated a fast exsolution process occurring within a few minutes, contributing to a notable electrochemical performance enhancement. Overall, reduction of the double perovskite system was shown to be an efficient method for bimetallic nanoparticle exsolution with the resulting La<sub>2-x</sub>NiRuO<sub>6-δ</sub> (x = 0.1 and 0.15) showing promise for electrocatalyst applications.

## 2. Results and Discussion

### 2.1. Stoichiometric and A-Site Deficient Lanthanum Nickel Ruthenate Double Perovskite

Stoichiometric lanthanum nickel ruthenate double perovskite with the nominal chemical formula La<sub>2</sub>NiRuO<sub>6</sub> (L2NR) and the A-site deficient compositions La<sub>2-x</sub>NiRuO<sub>6-δ</sub> were initially synthesized. Figure 1a shows the XRD patterns of the double perovskite samples and the reference La<sub>2</sub>NiRuO<sub>6</sub> (ICSD 96120).<sup>[36]</sup> The results of Le Bail refinement confirmed that the L2NR sample crystallized in the *P2<sub>1</sub>/n* space group with lattice parameters of *a* = 5.5656(1) Å, *b* = 5.6082(1) Å, *c* = 7.8772(2) Å, and β = 89.952(1)°. As shown in Figure 1b, the diffraction peaks of the L2NR sample corresponded well to the calculated Bragg positions. No secondary phases were observed within the resolution limits of the diffractometer. In addition, inductively coupled plasma optical emission spectrometry (ICP-OES) (Table S1, Supporting Information) showed that the cation ratio between La, Ni, and Ru was ≈2:1:1 as expected.

A-site nonstoichiometry has previously been reported to be essential for defect design and to facilitate exsolution of perovskite materials.<sup>[11,38]</sup> Thus L1.9NR and L1.85NR samples were synthesized with nominally 5 and 7.5 mol% A-site deficiency, respectively. XRD patterns of these samples (Figure 1a) indicated that L1.9NR and L1.85NR possessed the same crystal structure as the stoichiometric LNR, implying that lanthanum nickel ruthenate double perovskite structure remains stable with A-site deficiency up to at least 7.5 mol%. Higher concentrations of A-site deficiency led to excess NiO and RuO<sub>2</sub> secondary phases as shown in the XRD patterns in Figure S1, Supporting Information, suggesting that the accommodation of A-site deficiency is limited to concentrations of less than 10 mol%. Le Bail refinement results (Figure S2, Supporting Information) showed lattice volume shrinkage with increasing A-site deficiency caused by the loss of the large La<sup>3+</sup> cations and lattice distortion. ICP-OES results confirmed the increasing amount of A-site deficiency from L2NR to L1.85NR from the cation ratios in line with targeted stoichiometries (Table S1, Supporting Information).

Figure 1d–f shows the XPS spectra of Ni LMM Auger peaks, Ru 3d and O 1s core level of L2NR. The spectra were calibrated with O 1s oxygen–metal (O–M) peaks (binding energy, BE, at 529.2 eV), given that the adventitious C 1s peak overlaps the Ru 3d spectra and the O 1s O–M peak showed a relatively sharpened peak shape with FWHM = 1.1 eV. As Figure 1d shows, the Ni LMM Auger peak displays a specific peak shape with the peak maximum at 843.2 eV and a relatively broad peak (FWHM is ≈11.15 eV). The peak shapes and BE positions are consistent with previously reported Ni(II) compounds represented by the blue spectrum<sup>[37]</sup> in Figure 1d. Biesinger et al. reported that Ni(III) compounds would give rise to a unique peak at 832.8 eV in the Ni LMM Auger spectrum,<sup>[37]</sup> whereas in Figure 1d, no such characteristic peak was observed for the LNR sample, suggesting nickel cations are present as Ni<sup>2+</sup>. Regarding the ruthenium spectrum, the fitted BE of the Ru 3d<sub>5/2</sub> peak was 282.3 eV (Table S2, Supporting Information), which agrees with the

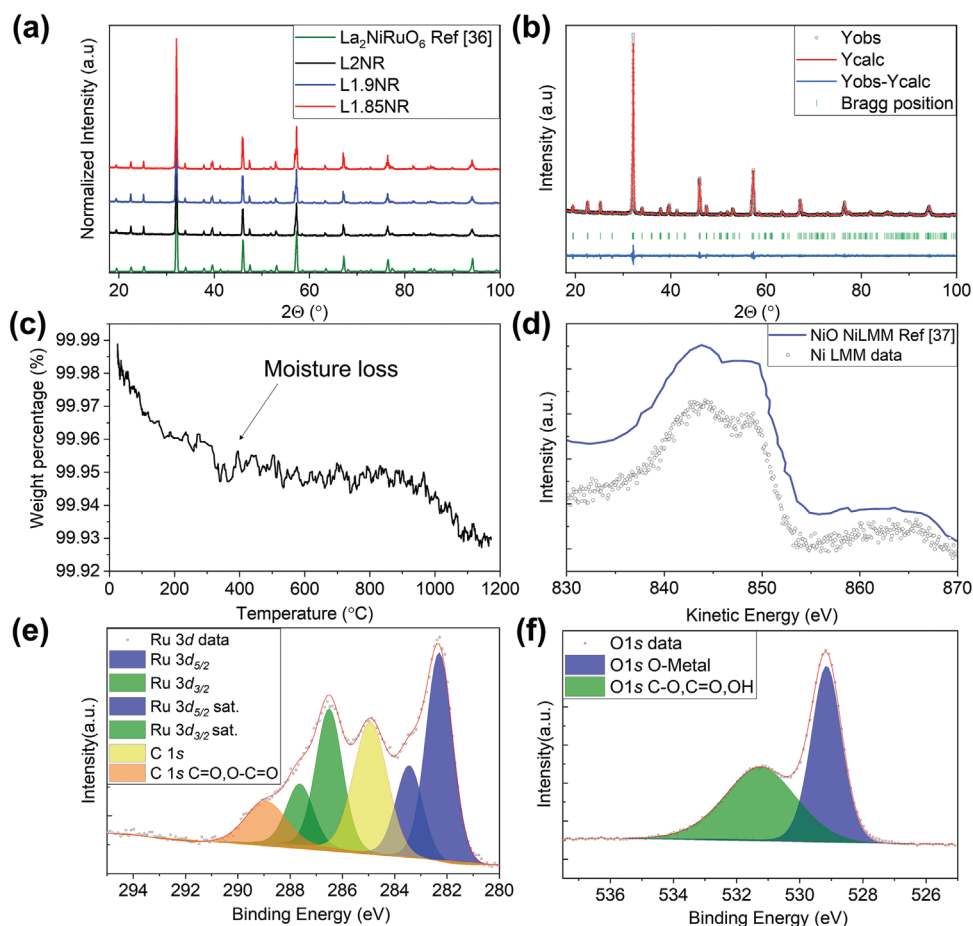


**Figure 1.** a) XRD patterns of as-prepared L2NR, L1.9NR, 1.85NR, and reference XRD pattern (ICSD 96120).<sup>[36]</sup> b) Le Bail refinement result calculated for as-prepared L2NR, where Yobs are the observed intensities, Ycalc the calculated intensities from the model, and Yobs–Ycalc the difference plot. The agreement indices are  $\chi^2 = 6.42$ ,  $R_p = 3.31\%$ ,  $R_{wp} = 4.56\%$ , and  $R_{exp} = 1.80\%$ . c) TGA plot of weight change (%) versus temperature. The first drop of 0.05% weight loss from room temperature to 300 °C is attributed to the loss of moisture and carbonates. d) XPS Ni LMM Auger spectrum of L2NR (black circles) and reference Ni LMM Auger peak of NiO (blue line).<sup>[37]</sup> e) XPS spectrum of Ru 3d orbitals of L2NR (black circles), fitted envelope plots (red line), and the fitting components (colored peaks). f) XPS spectrum of O 1s orbitals of L2NR (black circles), fitted envelope plots (red line), and the fitting components (colored peaks).

reported BE of the Ru 3d<sub>5/2</sub> peaks of the Ruddlesden–Popper phase LaSrNi<sub>0.5</sub>Ru<sub>0.5</sub>O<sub>4</sub>.<sup>[39]</sup> The doublet separation of the Ru 3d<sub>5/2</sub> and Ru 3d<sub>3/2</sub> peaks ( $\approx 4.2$  eV) indicated Ru<sup>4+</sup> cations were present in the LNR double perovskite.<sup>[39,40]</sup> Quantification of the Ru 3d and Ni LMM XPS spectra showed a 1.08:0.91 ratio between Ni and Ru cations (Table S2, Supporting Information), which agreed with the ICP-OES results. The A-site deficient samples, L1.9NR and L1.85NR, possessed similar XPS spectra to the L2NR composition, as reported in Figure S3, Supporting Information. The TGA plot of L2NR (Figure 1c) confirmed no mass gain/loss caused by redox of the B-site cation couple up to 800 °C. A 0.02 wt% mass loss was observed when the sample was heated to 1200 °C, attributed to the reduction of a modest amount of Ru<sup>4+</sup> ( $\approx 0.013$ at%). Combining the information from the techniques discussed above we can conclude that the L2NR, L1.9NR, and L1.85NR double perovskite phases crystallize with the monoclinic  $P2_1/n$  space group symmetry where Ni<sup>2+</sup> and Ru<sup>4+</sup> order at the B-site position.

## 2.2. Exsolution of A-site Deficient L2–xNR ( $x = 0.1$ and $0.15$ )

Figure 2 shows the SEM and TEM bright-field images of the L2–xNRs before and after reduction. Figure 2a,b confirmed homogeneity of the sample before reduction, and there were no nanoparticles present on the grain surface before the reduction process. After the reduction in wet 5% H<sub>2</sub>/Ar, both L1.9NR and L1.85NR samples contained exsolved nanoparticles (Figure 2c–f). However, after wet reduction, no obvious exsolution was observed from the L2NR sample (Figure S4, Supporting Information), thus confirming that the A-site deficiency is a critical driving force for the exsolution in the L2–xNR double perovskite system. The exsolution of metallic nanoparticles occurs via the destabilization of the parent perovskite lattice with high deficiencies in both the A-site, reported to facilitate a change in the equilibrium position, driving exsolution,<sup>[11]</sup> and oxygen positions.<sup>[13]</sup> The oxygen vacancy concentration increased when the A-site deficient sample (L2–xNR) was exposed to the 5%H<sub>2</sub>/Ar atmosphere. When the oxygen vacancy concentration exceeds



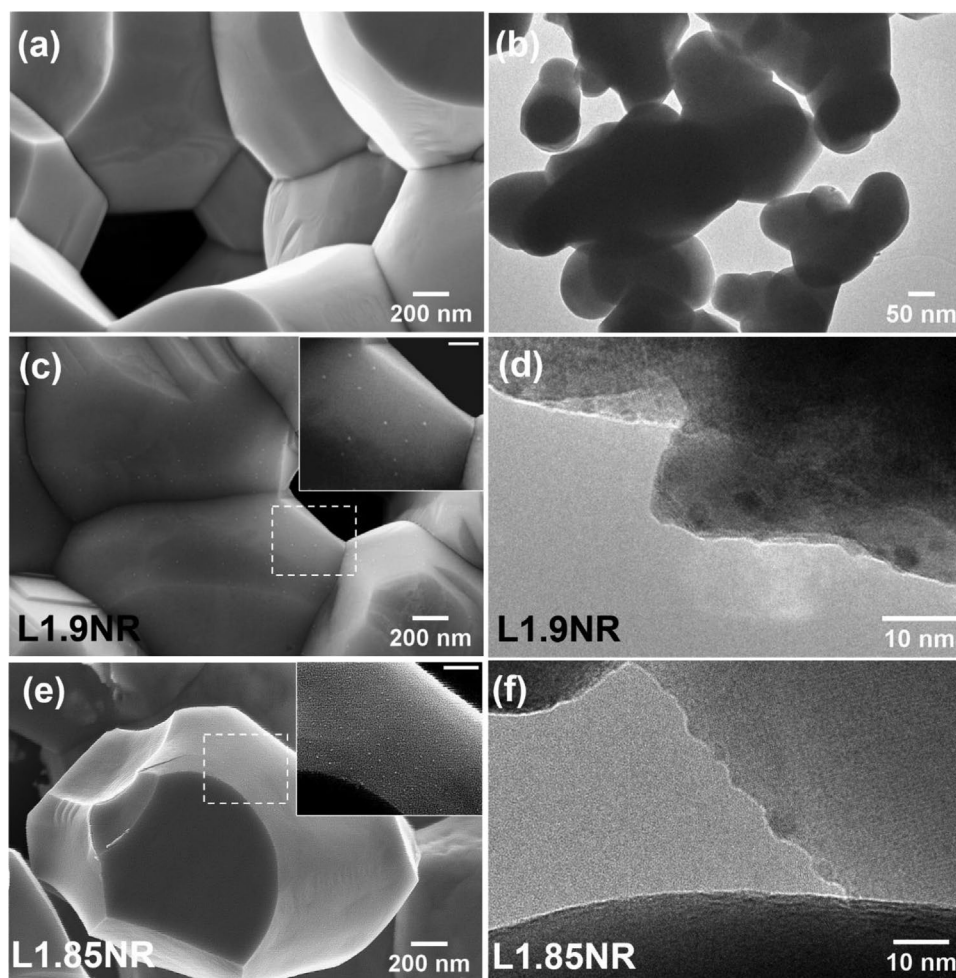
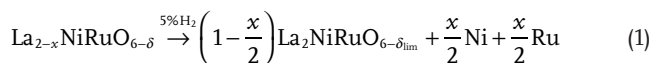


**Figure 2.** SEM (secondary electron imaging, SEI) and TEM bright-field images of a,b) stoichiometric double perovskite L2NR, c,d) 5 mol% A-site deficient phase L1.9NR, and e,f) 7.5 mol% A-site deficient phase L1.85NR after reduction in 5% $\text{H}_2/\text{Ar}$  at 450 °C for 3 h. The inset images (scale bar = 100 nm) show the morphology of reduced L1.9NR (c) and reduced L1.85NR (e) at higher magnification, highlighting the subtle nanoscale features.

the highest limit,  $\delta_{\text{lim}}$ , the materials go through a destabilization process, egressing metallic nanoparticles,<sup>[13]</sup> as shown in Equation (1):



From this expression, it is clear that the concentration of exsolved nanoparticles will be correlated with the A-site deficiency, and hence the highest exsolved nanoparticle concentration is expected in the L1.85NR sample. This offers the intriguing potential for manipulating nanoparticle exsolution through adjusting the “intrinsic” parameters (i.e., the concentration of A-site deficiency and B-site cation ratios), which would be an interesting area for further work. In the studies reported below, the L1.85NR sample is taken as an example for further investigation of the composition and morphology of the exsolved material.

Figure 3a shows the XPS Ru 3d spectra of the L1.85NR sample before and after reduction. The adventitious C 1s C–C peak is not apparent from the spectra profiles though it

is located at a BE position of 284.8–285.0 eV from analysis of the fitting results (Table S3, Supporting Information). Thus O 1s O–M was used for calibration of these two spectra as aforementioned. Compared to the as-prepared L1.85NR, the Ru 3d spectrum of the wet reduced sample displayed a distinct Ru 3d<sub>5/2</sub> peak at a 2 eV lower BE position, ascribed to the presence of metallic ruthenium. A C 1s O–C=O peak of increased intensity at 289.4 eV implied an increase in carbonate species that were absorbed and attached to the surface of the sample due to the exsolved nanoparticles. Regarding the Ni LMM Auger peak, due to the low intensity and signal to noise ratio, no evident peak evolution was shown in the acquired XPS spectrum (Figure S5, Supporting Information). Two secondary phase peaks at 44.5° and 44.1° two theta were observed in the XRD pattern of the wet-reduced L1.85NR sample, as shown in Figure 3b. The primary phase of L1.85NR remained as the  $P2_1/n$  monoclinic double perovskite structure, and the two small extra peaks were indexed to  $\text{Ni}_{0.32}\text{Ru}_{1.68}$   $P6_3/mmc$  hexagonal phase (ICSD 646325),<sup>[42]</sup> and  $\text{Ni}_{0.944}\text{Ru}_{0.056}$   $Fm-3m$  face centered cubic structure (ICSD 197164),<sup>[41]</sup> implying the formation of bimetallic exsolved nanoparticles.

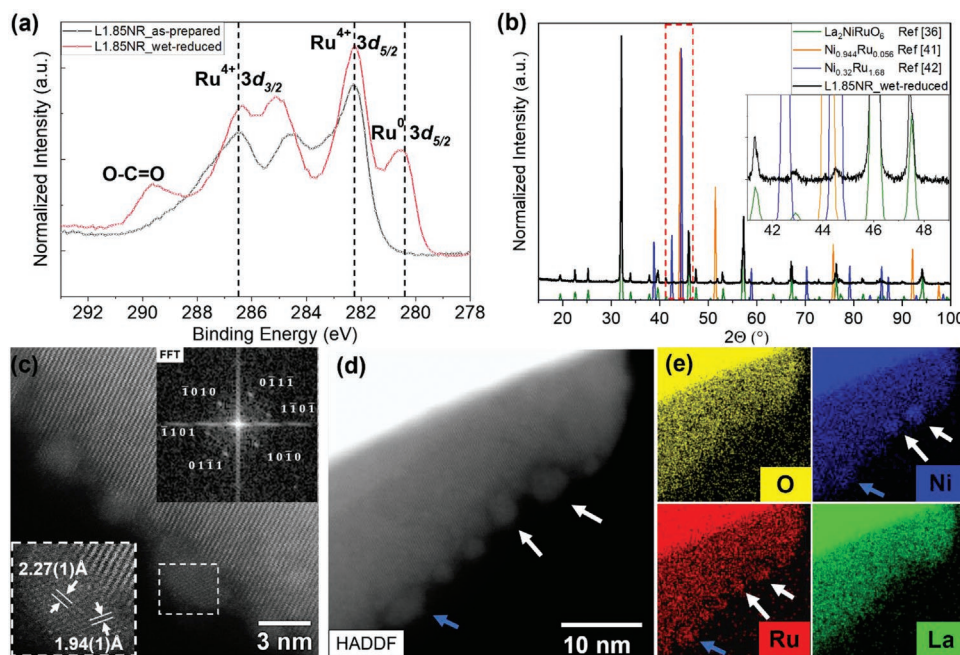


**Figure 3.** a) Comparison of XPS Ru 3d spectra of as-prepared L1.85NR sample (black) and reduced L1.85NR sample (red). The spectra were aligned by the lowest signal points at 278 eV and normalized by Ru<sup>4+</sup> 3d<sub>5/2</sub> peak area, given the Ru-content in the perovskite bulk was assumed to remain unchanged (Equation (1)). b) XRD pattern of reduced L1.85NR sample and reference patterns of La<sub>2</sub>NiRuO<sub>6</sub> (ICSD 96120),<sup>[36]</sup> Ni<sub>0.944</sub>Ru<sub>0.056</sub> (ICSD 194164),<sup>[41]</sup> and Ni<sub>0.32</sub>Ru<sub>1.68</sub> (ICSD 646325).<sup>[42]</sup> c) High-angle annular dark-field (HAADF) STEM image of exsolved nanoparticles on the surface of L1.85NR bulk. The inset image in the bottom-left corner is an enlarged view of the particle in the region indicated by the dashed rectangle to show the interplanar structure. The top-right inset is the Fast-Fourier-Transform (FFT) pattern from the same area with the lattice spacings indexed. The hcp particle is viewed along  $[\bar{1}2\bar{1}3]$  direction. d, e) HAADF image of exsolved nanoparticles and the corresponding EDX maps of La, Ni, Ru, and O elements.

HR-STEM and EDX were used to characterize the nanoscale morphology and chemical information of the wet-reduced L1.85NR. The STEM images in Figure 3c revealed that the size of the exsolved particles was about 3–4 nm in diameter. Furthermore, some particles were partially submerged into the bulk substrate, showing the “socketed” structure of exsolved nanoparticles and bulk substrate.<sup>[13–15,18]</sup> This socketed structure has been reported to give rise to high stability, poisoning resistance, and catalytic activity in the exsolved nanoparticles compared to conventional catalysts.<sup>[3,13,16]</sup> The Fast-Fourier-Transform (FFT) pattern, shown in the inset images in Figure 3c, can be indexed to the hexagonal close-packed (hcp) metal structure of the nanoparticle phase. The spacing of the FFT spots corresponds to real space interplanar spacings of 2.27(1) and 1.94(1) Å, attributed to the (10 $\bar{1}0$ ) and (0 $\bar{1}1\bar{1}$ ) planes of a Ni–Ru alloy with  $P6_3/mmc$  hexagonal lattice structure, in agreement with the XRD result. The zone-axis was indexed to the  $[\bar{1}2\bar{1}3]$  direction, with the angle between these two sets of fringes being 64° (Figure S6, Supporting Information). The 2% mismatch of the d-spacing compared to Ni<sub>0.94</sub>Ru<sub>0.056</sub> (ICSD-197164)<sup>[42]</sup> is attributed to the variable Ni and Ru content.

The STEM EDX mapping results shown in Figure 3e demonstrate a clear enrichment of both Ni and Ru signals detected from the exsolved nanoparticles, whereas no apparent La or O signal was observed. This confirmed that the observed nanoparticles originate from the exsolution of B-site cations (i.e., Ni and Ru cations), and the binary Ni–Ru alloy phase is formed during exsolution. In addition, a variation in the relative signal intensity for Ni and Ru was observed at different nanoparticle sites,

as shown in Figure 3e, which indicated that exsolved nanoparticles possess different Ni and Ru contents. Previously, Ni–Ru alloys with Ru content higher than 50 at% were reported to be the hcp phase.<sup>[43]</sup> The particle marked by the blue arrow has relatively lower Ni content and presents the hcp crystal structure in agreement with the XRD results. Correlating the local phase and composition distribution for individual exsolved particles with different A-site deficiencies would be an interesting area for future study.

### 2.3. Temperature- and Time-Dependent Exsolution Process

The high-temperature reduction has been commonly used to promote the exsolution process with facilitated diffusion of metal cations.<sup>[3,4,18,26,44–46]</sup> In this work, higher reduction temperature was found to cause phase degradation as the XRD patterns in Figure S7, Supporting Information, illustrate, with the double perovskite decomposing to lanthanum oxide, ruthenium oxide, nickel oxide, and a small amount of the metallic phases. A similar phenomenon was observed by Pavlova et al.,<sup>[47]</sup> where the Ni–Fe(Ru) nanocomposite with lanthanum oxide phase formed after reducing the LnFeNi(Ru) O<sub>3</sub> perovskite at 800 °C in H<sub>2</sub>. A lower temperature range (350–450 °C) was adopted in this study. Figures 4a–c show the bright-field images of the L1.85NR sample reduced at 450, 400, and 350 °C, respectively. Surprisingly, the L1.85NR sample reduced at 350 °C showed nicely distributed nanoparticles with a relatively uniform particle size of 2.2(5) nm in



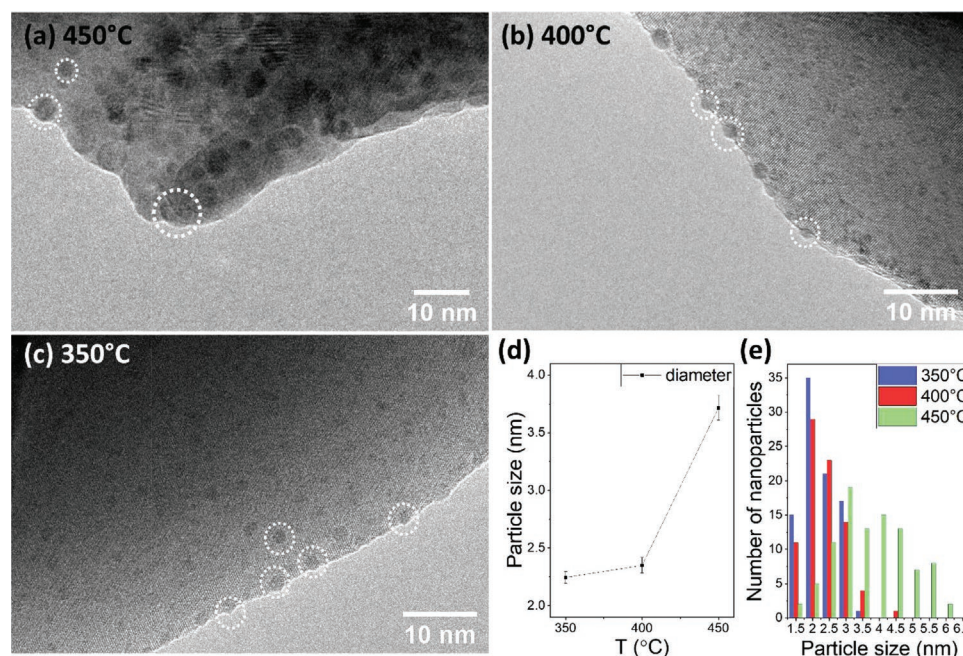


**Figure 4.** TEM images of L1.85NR reduced at a) 450, b) 400, and c) 350 °C and d,e) plot of particle size versus reduction temperature. For clarity, some exsolved particles in each of the TEM images are highlighted by white dashed circles. d) Particle size evolution with increasing temperature from 350 to 450 °C. The particle sizes are average values measured by ImageJ software from a total of 250 manually selected exsolved particles (70 for each temperature condition). Error bars represent the standard error of the average particle size. e) Particle size distribution of nanoparticles exsolved under different temperatures.

diameter. XRD patterns of the L1.85NR samples reduced at 400 and 350 °C both exhibited a secondary phase peak at 44.5°, suggesting a similar metallic phase ( $\text{Ni}_{0.32}\text{Ru}_{1.68}$ )<sup>[42]</sup> exsolved from the L1.85NR bulk (Figure S8, Supporting Information). STEM EDX mapping results obtained from L1.85NR reduced at 350 °C show ruthenium enrichment at most of the exsolved nanoparticles sites with little evidence of nickel-enrichment (Figure S9, Supporting Information), suggesting a high concentration of ruthenium in the exsolved nanoparticle after reduction at 350 °C.

It has been reported that exsolved particles tend to be smaller with higher particle density after reduction at a lower temperature.<sup>[48,49]</sup> This is consistent with our analysis from the L1.85NR samples, as shown in Figure 4a–c. Figure 4d,e demonstrates the average particle size and the particle size distribution of the L1.85NR sample reduced at different temperatures. From 350 to 400 °C, the average size of the exsolved particle was  $\approx 2.3$  nm ( $2.25 \pm 0.05$  nm at 350 °C and  $2.35 \pm 0.07$  nm at 400 °C, respectively), whereas when the reduction temperature increased to 450 °C, the particle size increased by  $\approx 1.5$  to  $3.72 \pm 0.11$  nm. The increased particle size indicates that the exsolved particles tend to grow significantly when the reduction temperature exceeds 400 °C, with smaller-sized nanoparticles seen at lower temperatures.<sup>[4]</sup> The size distribution also shows the increasing particle size with elevating reducing temperature, while the relatively broader size distribution of the sample reduced at 450 °C suggests that a fraction of small particles were also generated under this condition. In terms of the particle density, the TEM images provide a 2D image of the whole electron transparent area, and as Neagu et al. described,<sup>[14]</sup> it is challenging to distinguish the bulk substrate area where the exsolved particle is

attached. Further electron tomography investigation is needed to obtain accurate values for particle density.

To characterize the performance of L1.85NR and link changes in resistance with the progression of the exsolution process, in situ impedance spectroscopy was employed to investigate the exsolution process. Symmetric cells with as-prepared L1.85NR as the electrode were measured at open-circuit voltage during the reduction process. Compared to the spectrum measured before reduction (i.e., in the air), the spectrum measured after only 11 min (blue squares, marked by the red-black arrow in Figure 5a) started to curve due to the shrinking impedance arc, indicating a decrease in resistance, which suggested that exsolution had already occurred within 11 min of exposure to the reducing atmosphere. For longer times, the resistance continued to decrease until the reduction duration had reached 40 min, indicating a short area-specific resistance (ASR) relaxation time and high exsolution rate, which is comparable to the work reported by Gao et al.<sup>[50]</sup> Although the resistance is 30 times larger than state-of-the-art SOC electrodes, this suggests that the exsolution of Ni/Ru nanoparticles contributes to a significant enhancement of electrochemical performance (decrease from 291 to 29  $\Omega \text{ cm}^2$ ), as shown in Figure S10 and Table S4, Supporting Information. The significant enhancement of the ASR indicates that the exsolved nanoparticles on the surface of the electrode grains improve the density of triple-phase boundaries and the hydrogen oxidation kinetics. In contrast to reported time-dependent ASR data,<sup>[50]</sup> the ASR of the impedance spectra measured from 1 to 12 h shows a slight increase (Figure 5b and Table S4, Supporting Information) in the lower frequency part of the spectrum, which might relate to the loss of electronic conductivity, change of surface

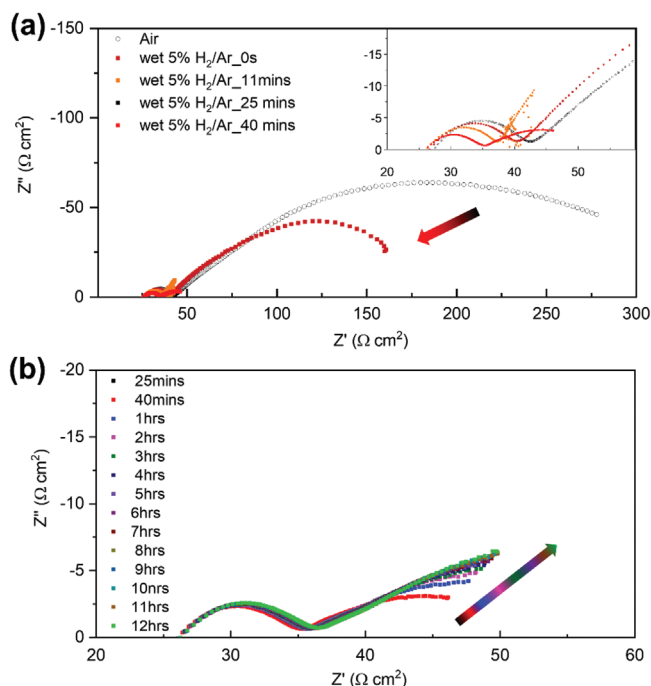


**Figure 5.** In situ impedance spectra of the symmetric cell measured in air and humidified 5%  $\text{H}_2/\text{Ar}$  for different dwell times: a) 0, 11, 25, and 40 min, and b) from 25 min to 13 h.

oxygen stoichiometry, and loss of active surface during particle growth. The electrochemical performance of the symmetric cell would be further improved by adjusting the cell structure, electrode microstructure, electrode composition, and grading in future work. In general, the EIS results manifest the potential applications of these materials, including applying them as electrodes in solid oxide fuel cells and solid-oxide electrolyzers and mixing with highly conductive materials for electrocatalytic optimization.

The exsolution process usually involves four steps: exposure to reducing conditions, nucleation of the metallic phase, ion migration, and particle growth. As the process involves the spontaneous destabilization of the parent perovskite lattice in a reducing atmosphere, the A-site deficiency in our double perovskite structure provides the driving force of the exsolving B-site cations by the tendency to re-establish A-site stoichiometry, as Equation (1) shows. Both nickel and ruthenium are proven to be reduced to metallic phases,<sup>[18]</sup> while nickel exsolution usually occurs at high temperatures ( $>600\text{ }^\circ\text{C}$ ).<sup>[2,22,51,52]</sup> At the lower temperature,  $350\text{ }^\circ\text{C}$ , more ruthenium was expected to be exsolved from the bulk (Figure S9, Supporting Information). However, in multiple cation systems, it has been reported that introducing more reducible ions would lower the segregation energy.<sup>[10]</sup> Hence, nickel exsolution driven by A-site deficiency can be further promoted in the double perovskite system by mixing with platinum-group elements (e.g., Rh, Pd, and Ru).<sup>[10,18]</sup> Thus, when the reduction temperature was increased to  $450\text{ }^\circ\text{C}$ , the formation of Ni–Ru bimetallic nanoparticles was promoted during the exsolution from L1.85NR (Figure 3). Based on our results, the exsolution process is proposed to explain the mechanism of Ni/Ru alloy nanoparticles exsolving

from the L1.85NR sample, as illustrated in Figure 6. Nickel and ruthenium occupy octahedral sites with rock-salt ordering, according to the  $P2_1/n$  lattice structure confirmed with the Le Bail refinement result (Figure 1b). Oxygen vacancies are introduced into the double perovskite lattice by exposure to wet 5%  $\text{H}_2/\text{Ar}$ , and the presence of A-site deficiency promotes the formation of oxygen vacancies and B-site cations then segregate from the bulk to the surface and form alloy nuclei. DFT calculations performed by Kwon et al.<sup>[52]</sup> have confirmed that segregation of nickel and ruthenium cations occurs preferentially on the surface rather than in the bulk due to a lower Gibbs free energy change. As the in situ EIS result suggested (Figure 5), the first two stages (Figure 6) can be achieved in the first few minutes of the reduction. For the latter stage of the exsolution, Gao et al.<sup>[2]</sup> proposed three key factors affecting particle growth: strain, amount of reactant, and ion diffusion. In this case, both nickel and ruthenium are abundantly and homogeneously distributed through the bulk double perovskite lattice. Furthermore, as shown in Figure 4d, the particles grow with increasing reduction temperature, which implies the growth is affected by thermally activated ion diffusion. In this study, we have demonstrated that, from A-site deficient double perovskite oxides, the exsolution process happens at a relatively lower temperature and forms smaller Ni–Ru bimetallic nanoparticles, which in principle can provide better electrochemical performance for a range of applications.

### 3. Conclusion

In this work, a new system for exsolution of bimetallic nanoparticles, lanthanum nickel ruthenate double perovskite ( $\text{La}_{2-x}\text{NiRuO}_{6-\delta}$ ,  $x = 0, 0.1, \text{ and } 0.15$ ), has been investigated. The parent double perovskite adopted a  $P2_1/n$  monoclinic structure with  $\text{Ni}^{2+}$  and  $\text{Ru}^{4+}$  ordering at the B-site position. After reducing in humid 5%  $\text{H}_2/\text{Ar}$ , the A-site deficient samples L1.9NR and L1.85NR samples exsolved nanoparticles at  $450\text{ }^\circ\text{C}$ , indicating that A-site deficiency facilitated exsolution. XPS, XRD, HR-TEM, and STEM-EDX revealed that the exsolved nanoparticles were Ni–Ru alloy phases. The dependence on temperature and time of the exsolution were further investigated. The exsolved nanoparticles become larger for increased reduction temperature, suggesting a diffusion-limited particle growth. In addition, this double perovskite with 7.5 mol% A-site deficiency was found to exsolve small nanoparticles even at  $350\text{ }^\circ\text{C}$ . In situ EIS results showed that exsolution happened within the first 11 min of reduction. The resistance of the symmetric cell decreased drastically from 291 to  $29\text{ }\Omega\text{ cm}^2$  during the exsolution process, indicating the significant enhancement of electrochemical performance achieved with Ni–Ru exsolution of L1.85NR materials.

### 4. Experimental Section

**Sample Preparation:** The  $\text{La}_{2-x}\text{NiRuO}_{6-\delta}$  ( $x = 0, 0.1, \text{ and } 0.15$ , denoted as L2-xNR) double perovskites were synthesized by the citrate-nitrate sol–gel method.<sup>[53]</sup> Amounts of  $\text{La}(\text{NO}_3)_3 \cdot 6\text{H}_2\text{O}$  (Sigma-Aldrich, 99.999%),  $\text{Ni}(\text{NO}_3)_2 \cdot 6\text{H}_2\text{O}$  (Sigma-Aldrich, 99.999%), and



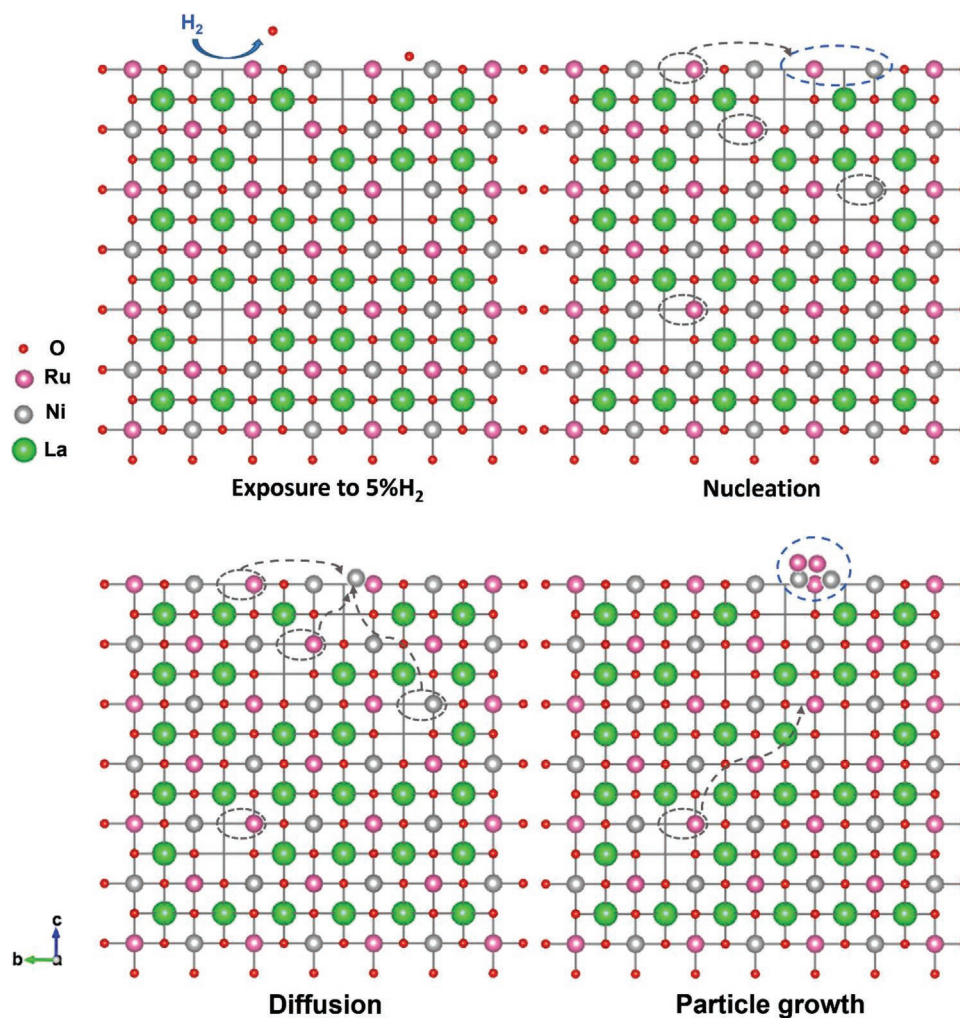


**Figure 6.** Schematic illustration of the exsolution process of Ni–Ru bimetallic nanoparticles from A-site deficient double perovskite L1.85NR. Cubic lattice structures are sketched and viewed along with the [100] direction.

Ru(NO)(NO<sub>3</sub>)<sub>x</sub>(OH)<sub>y</sub> solution (Johnson Matthey, 99.8%) were mixed in citric acid solution (10 wt%, VWR chemicals). The solution was stirred and heated on a hotplate to evaporate water until the gelation process started. The gel was further dried at 300 °C, then decomposed at 600 °C at 12 h in static air to form a black precursor mixture. The resulting mixture was calcined at 1100 °C for 12 h in static air to form the double perovskite products. Subsequently, the double perovskites were reduced in wet 5% hydrogen/argon (≈3% H<sub>2</sub>O content achieved by passing gas through a water bubbler) at selected temperatures for 3 h.

**Cell Fabrication:** The dense pellets of (La<sub>0.9</sub>Sr<sub>0.1</sub>)<sub>0.98</sub>Ga<sub>0.8</sub>Mn<sub>0.2</sub>O<sub>3-δ</sub> (LSGM) electrolyte were fabricated by pressing LSGM commercial powder (Praxair Inc., USA) into 13 mm diameter pellets and then sintering at 1400 °C for 8 h, followed by grinding and annealing. The L2-xNR electrode ink was prepared through ball-milling, vacuum drying, and triple-roll milling. The synthesized double perovskite powder (L1.85NR), which was dispersed in acetone, was placed into a high-energy ball mill to obtain a nanoscaled ink. Then vacuum drying was adopted to ensure complete removal of any residual organic solvent. The product powder and ink vehicles (commercial ink vehicle FCM R1835, Fuelcellmaterials Inc., USA) were manually mixed with a weight ratio of 2:1. Triple-roll milling was used to thoroughly disperse the electrode powder in the ink vehicle and eliminate aggregates. Screening printing of the electrode ink onto the electrolyte pellet was conducted by creating a mask of scotch tape with a 6 mm hole attached to the LSGM pellet surface, then brush painting a layer of electrode ink on to the

surface. After drying the ink, the mask was removed, and the electrode layer was sintered on to the electrolyte at 1000 °C for 6 h. An electrolyte ink was prepared using the same method as the electrode ink and then deposited on a LSGM electrolyte by heat treatment at 1000 °C for 1.5 h before adding the L1.85NR electrode layer.<sup>[54]</sup> Silver paste, as a current collector (Alfa Aesar) was painted on the surface of the electrode and annealed at 700 °C for 2 h.

**Characterization:** XRD was applied to investigate the phases of samples before and after reduction using a PANalytical MPD diffractometer with Cu K<sub>α</sub> radiation. Le Bail refinement was implemented using the FullProf software suite<sup>[55]</sup> to obtain the double perovskite crystal structure and lattice parameters. XPS spectra were acquired using a high-throughput Thermo Fisher K-alpha spectrometer with monochromatic Al K<sub>α</sub> X-ray source ( $h\nu = 1486.6$  eV) to derive compositional and chemical information of the materials. The spot size was 400 μm<sup>2</sup>, and a flood gun was operating during acquisition. Avantage software was used to analyze the peak components of XPS spectra, and all spectra were calibrated by setting the O 1s peak to the BE position of 529.2 eV. ICP-OES (Thermo Scientific iCAP 6000 Series ICP spectrometer) was applied to characterize the cation ratio of the synthesized materials. An SEM (Zeiss Leo Gemini 1525) was used to characterize the microstructure of symmetric cells and the morphology of double perovskite samples before and after reduction. TEM was used to determine the morphology and size of the exsolved nanoparticles. A JEOL JEM-2100F microscope operated at 200 kV was used to obtain the bright-field images of the sample before and after

reduction. The high-resolution HAADF-STEM imaging and EDS elemental mapping were performed using a Thermo Fisher Titan STEM (G2 80-200) equipped with a Cs probe corrector (CEOS), a ChemiSTEM Super-X EDX detector, and a HAADF detector operating with an inner angle of 55 mrad at 200 kV. The incident electron beam convergence angle was 21 mrad. To prepare the samples, LxNR powder samples were dispersed in isopropanol by ultrasonication for 20 min and drop-cast onto holey carbon-coated copper TEM grids. The acquired images were analyzed by ImageJ software (<https://imagej.nih.gov>) to derive the lattice spacing and size of the nanoparticles. The performance of the symmetrical cell (L1.85NR/LSGM-interlayer/LSGM/LSGM-interlayer/L1.85NR) was measured by EIS at 450 °C to investigate the process of exsolution. Two-probe geometry was implemented with two Pt mesh current collectors attached to the opposite sides of symmetrical cell samples. The configuration was connected to a frequency response analyzer (Solartron Modulab XM ECS) with a frequency range from 1 MHz to 50 mHz. The impedance spectra were measured before and after supplying 5% H<sub>2</sub>/Ar gas to the symmetrical cell. The Zview software (Version 3.5 by Scribner Associates, USA) was used to analyze acquired EIS spectra. TGA (Netzsch STA 449c F5) was used to understand the material stability as a function of temperature under a flowing compressed air atmosphere. Following a correction run with an empty crucible, ≈40 mg of sample was loaded into a Pt crucible, and the sample was heated to 1200 °C at a rate of 10 °C min<sup>-1</sup>. The change in mass was subsequently analyzed using Netzsch Proteus software.

## Supporting Information

Supporting Information is available from the Wiley Online Library or from the author.

## Acknowledgements

TEM access was supported by the Henry Royce Institute for Advanced Materials, funded through EPSRC grants EP/R00661X/1, EP/S019367/1, EP/P025021/1, and EP/P025498/1. S.J.H. acknowledges the European Research Council (ERC) under the European Union's Horizon 2020 research and innovation programme (Grant ERC-2016-STG-EvoluTEM-715502). R.C. and S.J.H. would like to thank the UK Catalysis Hub for resources and support provided via the membership of the UK Catalysis Hub Consortium and funded by EPSRC grant: EP/R027129/1. G.E.W. acknowledges the EPSRC CDT in Fuel Cells and their Fuels (EP/L015749/1).

## Conflict of Interest

The authors declare no conflict of interest.

## Data Availability Statement

The data that support the findings of this study are available from the corresponding author upon reasonable request.

## Keywords

bimetallic nanoparticles, double perovskites, Ni–Ru alloys, low-temperature exsolution

Received: November 14, 2021

Revised: January 7, 2022

Published online: February 19, 2022

- [1] J. Myung, D. Neagu, D. N. Miller, J. T. S. Irvine, *Nature* **2016**, 537, 528.
- [2] Y. Gao, D. Chen, M. Saccoccio, Z. Lu, F. Ciucci, *Nano Energy* **2016**, 27, 499.
- [3] E. Cali, G. Kerherve, F. Naufal, K. Kousi, D. Neagu, E. I. Papaioannou, M. P. Thomas, B. S. Guiton, I. S. Metcalfe, J. T. S. Irvine, D. J. Payne, *ACS Appl. Mater. Interfaces* **2020**, 12, 37444.
- [4] C. Tang, K. Kousi, D. Neagu, J. Portolés, E. I. Papaioannou, I. S. Metcalfe, *Nanoscale* **2019**, 11, 16935.
- [5] V. Kruefu, U. Inpan, P. Leangtanom, C. Arkarviphath, P. Kongpark, D. Phokharatkul, A. Wisitorsaot, A. Tuantranont, S. Phanichphant, *Phys. Status Solidi A* **2018**, 215, 1701015.
- [6] G. Chen, S. Desinan, R. Rosei, F. Rosei, D. Ma, *Chem. - Eur. J.* **2012**, 18, 7925.
- [7] S. Li, D. Gong, H. Tang, Z. Ma, Z. T. Liu, Y. Liu, *Chem. Eng. J.* **2018**, 334, 2167.
- [8] F. Tao, *Chem. Soc. Rev.* **2012**, 41, 7977.
- [9] O. Kwon, S. Joo, S. Choi, S. Sengodan, G. Kim, *J. Phys. Energy* **2020**, 2, 032001.
- [10] C. Tang, K. Kousi, D. Neagu, I. S. Metcalfe, *Chem. - Eur. J.* **2021**, 27, 6666.
- [11] D. Neagu, G. Tsekouras, D. N. Miller, H. Ménard, J. T. S. S. Irvine, *Nat. Chem.* **2013**, 5, 916.
- [12] J. Zhang, M. R. Gao, J. L. Luo, *Chem. Mater.* **2020**, 32, 5424.
- [13] D. Neagu, T. S. Oh, D. N. Miller, H. Ménard, S. M. Bukhari, S. R. Gamble, R. J. Gorte, J. M. Vohs, J. T. S. Irvine, *Nat. Commun.* **2015**, 6, 8120.
- [14] D. Neagu, V. Kyriakou, I. L. Roiban, M. Aouine, C. Tang, A. Caravaca, K. Kousi, I. Schreuer-Piet, I. S. Metcalfe, P. Vernoux, M. C. M. Van De Sanden, M. N. Tsampas, *ACS Nano* **2019**, 13, 12996.
- [15] T. S. Oh, E. K. Rahani, D. Neagu, J. T. S. Irvine, V. B. Shenoy, R. J. Gorte, J. M. Vohs, *J. Phys. Chem. Lett.* **2015**, 6, 5106.
- [16] H. Han, J. Park, S. Y. Nam, K. J. Kim, G. M. Choi, S. S. P. Parkin, H. M. Jang, J. T. S. Irvine, *Nat. Commun.* **2019**, 10, 1471.
- [17] P. Steiger, D. Burnat, H. Madi, A. Mai, L. Holzer, J. Van Herle, O. Kröcher, A. Heel, D. Ferri, *Chem. Mater.* **2019**, 31, 748.
- [18] K. Kousi, C. Tang, I. S. Metcalfe, D. Neagu, *Small* **2021**, 17, 2006479.
- [19] K. Kousi, D. Neagu, L. Bekris, E. I. Papaioannou, I. S. Metcalfe, *Angew. Chem., Int. Ed.* **2020**, 59, 2510.
- [20] L. Kapokova, S. Pavlova, R. Bunina, G. Alikina, T. Krieger, A. Ishchenko, V. Rogov, V. Sadykov, *Catal. Today* **2011**, 164, 227.
- [21] S. Ding, M. Li, W. Pang, B. Hua, N. Duan, Y. Q. Zhang, S. N. Zhang, Z. Jin, J. L. Luo, *Electrochim. Acta* **2020**, 335, 135683.
- [22] Y. F. Sun, J. H. Li, L. Cui, B. Hua, S. H. Cui, J. H. Li, J. L. Luo, *Nanoscale* **2015**, 7, 11173.
- [23] T. Tan, M. Qin, K. Li, M. Zhou, T. Liu, C. Yang, M. Liu, *Int. J. Hydrogen Energy* **2020**, 45, 29407.
- [24] K. Shao, F. Li, G. Zhang, Q. Zhang, K. Maliutina, L. Fan, *ACS Appl. Mater. Interfaces* **2019**, 11, 27924.
- [25] Y. Song, H. Li, M. Xu, G. Yang, W. Wang, R. Ran, W. Zhou, Z. Shao, *Small* **2020**, 16, 2001859.
- [26] K. Kousi, D. Neagu, L. Bekris, E. Cali, G. Kerherve, E. I. Papaioannou, D. J. Payne, I. S. Metcalfe, *J. Mater. Chem. A* **2020**, 8, 12406.
- [27] Y. Liu, Z. Wang, Y. Zhong, X. Xu, J. P. M. Veder, M. R. Rowles, M. Saunders, R. Ran, Z. Shao, *Chem. Eng. J.* **2020**, 390, 124645.
- [28] J. S. Jang, J. K. Kim, K. Kim, W. G. Jung, C. Lim, S. Kim, D. H. Kim, B. J. Kim, J. W. Han, W. C. Jung, I. D. Kim, *Adv. Mater.* **2020**, 32, 2003983.
- [29] M. A. Naeem, D. B. Burueva, P. M. Abdala, N. S. Bushkov, D. Stoian, A. V. Bukhtiyarov, I. P. Prosvirnin, V. I. Bukhtiyarov, K. V. Kovtunov, I. V. Koptuyug, A. Fedorov, C. R. Müller, *J. Phys. Chem. C* **2020**, 124, 25299.

- [30] M. Buharon, S. Singh, E. P. Komarala, B. A. Rosen, *CrystEngComm* **2018**, *20*, 6372.
- [31] L. Deng, F. Hu, M. Ma, S. Huang, Y. Xiong, H. Chen, L. Li, S. Peng, *Angew. Chem.* **2021**, *133*, 22450.
- [32] S. Mehravar, S. Fatemi, M. Komiyama, *Int. J. Energy Res.* **2020**, *44*, 8000.
- [33] G. Chen, S. Desinan, R. Rosei, F. Rosei, D. Ma, *Chem. Commun.* **2012**, *48*, 8009.
- [34] Y. Qin, X. Bai, *Fuel* **2022**, *307*, 121921.
- [35] H. Wang, Y. Yang, F. J. Disalvo, H. D. Abrunā, *ACS Catal.* **2020**, *10*, 4608.
- [36] K. Yoshii, H. Abe, M. Mizumaki, H. Tanida, N. Kawamura, *J. Alloys Compd.* **2003**, *348*, 236.
- [37] M. C. Biesinger, L. W. M. Lau, A. R. Gerson, R. S. C. Smart, *Phys. Chem. Chem. Phys.* **2012**, *14*, 2434.
- [38] H. Arandiyān, S. S. Mofarah, C. C. Sorrell, E. Doustkhah, B. Sajjadi, D. Hao, Y. Wang, H. Sun, B.-J. Ni, M. Rezaei, Z. Shao, T. Maschmeyer, *Chem. Soc. Rev.* **2021**, *50*, 10116.
- [39] M. Lü, X. Deng, J. C. Waerenborgh, X. Wu, J. Meng, *Dalton Trans.* **2012**, *41*, 11507.
- [40] D. J. Morgan, *Surf. Interface Anal.* **2015**, *47*, 1072.
- [41] E. Raub, D. Menzel, *Int. J. Mater. Res.* **1961**, *52*, 831.
- [42] I. I. Kornilov, K. P. Myasnikova, *Russ. Metal. Mining* **1964**, *4*, 95.
- [43] S. Hallström, *J. Phase Equilib. Diffus.* **2004**, *25*, 252.
- [44] H. Lv, L. Lin, X. Zhang, Y. Song, H. Matsumoto, C. Zeng, N. Ta, W. Liu, D. Gao, G. Wang, X. Bao, *Adv. Mater.* **2020**, *32*, 1906193.
- [45] H. Arandiyān, Y. Wang, J. Scott, S. Mesgari, H. Dai, R. Amal, *ACS Appl. Mater. Interfaces* **2018**, *10*, 16352.
- [46] O. Kwon, S. Sengodan, K. Kim, G. G. G. Kim, H. Y. Jeong, J. Shin, Y. W. Ju, J. W. Han, G. G. G. Kim, *Nat. Commun.* **2017**, *8*, 15967.
- [47] S. Pavlova, L. Kapokova, R. Bunina, G. Alikina, N. Sazonova, T. Krieger, A. Ishchenko, V. Rogov, R. Gulyaev, V. Sadykov, C. Mirodatos, *Catal. Sci. Technol.* **2012**, *2*, 2099.
- [48] V. Kyriakou, D. Neagu, G. Zafeiropoulos, R. K. Sharma, C. Tang, K. Kousi, I. S. Metcalfe, M. C. M. Van De Sanden, M. N. Tsampas, *ACS Catal.* **2020**, *10*, 1278.
- [49] S. K. Otto, K. Kousi, D. Neagu, L. Bekris, J. Janek, I. S. Metcalfe, *ACS Appl. Energy Mater.* **2019**, *2*, 7288.
- [50] Y. Gao, Z. Lu, T. L. You, J. Wang, L. Xie, J. He, F. Ciucci, *J. Phys. Chem. Lett.* **2018**, *9*, 3772.
- [51] W. Kobsiriphat, B. D. Madsen, Y. Wang, M. Shah, L. D. Marks, S. A. Barnett, *J. Electrochem. Soc.* **2010**, *157*, B279.
- [52] O. Kwon, K. Kim, S. Joo, H. Y. Jeong, J. Shin, J. W. Han, S. Sengodan, G. Kim, *J. Mater. Chem. A* **2018**, *6*, 15947.
- [53] C. Y. Tsai, C. M. McGilvery, A. Aguadero, S. J. Skinner, *Int. J. Hydrogen Energy* **2019**, *44*, 31458.
- [54] M. A. Yattoo, A. Aguadero, S. J. Skinner, *APL Mater.* **2019**, *7*, 013204.
- [55] J. Rodríguez-Carvajal, *Phys. B* **1993**, *192*, 55.